COMPARISON OF FEATURE BASED SEGMENTATION OF SAR SATELLITE SEA ICE IMAGES WITH MANUALLY DRAWN ICE CHARTS

Mari-Ann N. Moen[1], Anthony P. Doulgeris[1], Stian N. Anfinsen[1], Nick Hughes[2], Angelika H.H. Renner[3], Sebastian Gerland[3], Trond Robertsen[2], Vera Lund[2], and Torbjørn Eltoft[1,4]

[1]*University of Tromsø, The Auroral Observatory, 9037 Tromsø, Norway, e-mail: Mari-Ann.Moen@uit.no*
[2]*Norwegian Sea Ice Service, Norwegian Meteorological Institute, P-box 6314, 9293 Tromsø, Norway*
[3]*Norwegian Polar Institute, FRAM centre, 9296 Tromsø, Norway*
[4]*Northern Research Institute, Norway*

ABSTRACT

This paper explores automatic segmentation of synthetic aperture radar (SAR) satellite images of sea ice. The investigation is based on a comparison of an automatically segmented SAR image and manual classifications by ice service analysts. The automatic algorithm uses statistical properties of the backscattered radar signals to segment the SAR image into a given number of classes. The numberof classes is determined from available ground truth. Sea ice experts, aided by various in-situ data, were able to label most of the segments from the automatic algorithm. We utilized the physical information in the polarimetric features used in the classification algorithm, in order to further explore the class labeling.

1. INTRODUCTION

Classification of sea ice into types in SAR images is a demanding task due to the complexity of the medium, its dynamics and dependence of weather and imaging conditions. Especially in the polar areas, the limited availability of in-situ data makes it difficult to evaluate the results. The Norwegian Ice Service produces ice charts of sea ice concentration, based on SAR and optical images, but have less experience with classifying ice according to sea ice types, distinguished by age, thickness and/or deformation level. Automating sea ice segmentation would make the classification more efficient and less analyst dependent.
In this study a comparison between two manually drawn ice charts and an automatically segmented image of the polarimetric scene is performed. Ground truth and some polarimetric features are utilized to validate/classify the segments into ice types. Sea ice experts labeled the segments in the automated segmentation aided by optical photos, thickness data and the Pauli image, which visualizes polarimetric data as an RGB image [1]. For some segment types the sea ice experts were not able to distinguish the segments found by the automatic algorithm. To verify their labeling and explore the non-distinguishable segments we exploited the physical information in the polarimetric features used in the segmentation algorithm.

Ground truth data were collected during a field campaign in the marginal ice zone area north of Svalbard in the first two weeks of April 2011. Radarsat-2 (quad-polarization fine and dual polarization medium resolution, C-band), and TerraSAR-X (single and dual-polarization, X-band) scenes were co-located in time and space with in-situ measurements (snow and ice thickness, ice drift, conductivity, temperature, snow grain size and density) and helicopter-borne electromagnetic induction measurements of ice plus snow thickness (EM-bird flights). In addition to the EM-bird, a camera was mounted at the helicopter to give optical photos along the helicopter track.

A similar study to ours was done by [2]. They explore polarimetric parameters for ice type and open water discrimination, by investigating the classification power of single parameters and combinations of two and three parameters. They identify three ice classes characterized by roughness. In our study we characterize and identify five classes in terms of thickness and ice type. Some of the polarimetric parameters included are similar to ours, in addition they have investigated various decompositions.
This paper is organized as follows: Sec. 2 describes the available dataset and the experiment. In Sec. 3 we present our result of the intercomparison of the manual and the automatic segmentation together with the validation and interpretation of the latter. Our conclusions are given in Sec. 5.

2. METHODS

2.1. The Dataset

The study area comprised first-year sea ice at different stages of development and leads, both open and refrozen, located north of Svalbard. Two main categories of data were aquired; ground truth data and satellite-borne SAR

data.

Ground truth: Ice thickness measurements over a large area were performed by a helicopter-borne electromagnetic induction sounder (EM-bird)[3]. These flights were also used to collect optical photos and roughness measurements with a laser altimeter. An Iridium Surface Velocity Profiler (SVP) buoy was deployed onto the ice on 11 of April. This buoy transmits its position hourly together with other parameters and can be used for drift calculations. GPS trackers were placed on the ice on 12 of April to track the ice drift occuring between and during the EM-Bird flight and satellite image aquisition. In addition, regular sea ice shipboard observations and photographs from the ship were performed.

Satellite scenes: This study only uses the quad-polarization fine mode Radarsat-2 image from 12 April, whose location, north of Svalbard, is shown in Fig. 1. This image coincides with a good collection of ground truth data. Another advantage is the timing of the helicopter flight and the Radarsat-2 overpass: only 1 h 46 min from the image acquisition till the end of the EM-bird measurements, which contributes to an accurate drift correction. Analysis of overlapping Radarsat-2 (dual-pol ScanSAR wide) and TerraSAR-X (single-pol scanSAR) images form the same is delayed to a subsequent study.

Figure 1. Location of Radarsat-2 image, 12 April 2011. Red box north of Svalbard (center 81.1^oN 19.1^oE*).*

2.2. The Experiment

The Automatic segmentation

The single-look complex (SLC) data from the Radarsat-2 image were multilooked, using 21 by 21 looks, to create multilook complex (MLC) data in covariance matrix format. Six empirical real-valued features were then extracted from the MLC data using the Extended Polarimetric Feature Space method (EPFS method) [4]. The non-Gaussianity feature (eq. 3) is an exception, as it uses both SLC and MLC data and is calculated in the same step as the covariance matrix. Given a local neighbourhood of SLC vectors ($\mathbf{s} = [S_{hh}\ \frac{1}{\sqrt{2}}(S_{hv} + S_{vh})\ S_{vv}]^T$), the covariance matrix is calculated as:

$$\mathbf{C} = \frac{1}{N}\sum_{i=1}^{L} \mathbf{s}_i \mathbf{s}_i^H \tag{1}$$

where

$$\mathbf{C} = \begin{bmatrix} \left\langle |S_{HH}|^2 \right\rangle & \langle S_{HH} S_{HV}^* \rangle & \langle S_{HH} S_{VV}^* \rangle \\ \langle S_{HV} S_{HH}^* \rangle & \left\langle |S_{HV}|^2 \right\rangle & \langle S_{HV} S_{VV}^* \rangle \\ \langle S_{VV} S_{HH}^* \rangle & \langle S_{VV} S_{HV}^* \rangle & \left\langle |S_{VV}|^2 \right\rangle \end{bmatrix}. \tag{2}$$

The operators $(\cdot)^T$ and $(\cdot)^H$ define the ordinary and the Hermitian transpose operations respectively, and $\langle\cdot\rangle$ is the sample mean over all single-look measurements. The equations defining the features are given in Eqs. (3) - (8), where $d = 3$ is the dimension of the SLC vector.

Relative kurtosis/non-Gaussianity:

$$RK = \frac{1}{Nd(d+1)} \sum_{i=1}^{N} \left[\mathbf{s}_i^H \mathbf{C}^{-1} \mathbf{s}_i\right]^2. \tag{3}$$

Geometric brightness:

$$B = \sqrt[d]{det(\mathbf{C})}. \tag{4}$$

Co-polarization ratio:

$$R_{hh/vv} = \frac{\langle S_{HH} S_{HH}^* \rangle}{\langle S_{VV} S_{VV}^* \rangle}. \tag{5}$$

Cross-polarization ratio:

$$R_{hv/B} = \frac{\langle S_{HV} S_{HV}^* \rangle}{B}. \tag{6}$$

Co-polarization correlation magnitude:

$$|\rho| = \left| \frac{\langle S_{HH} S_{VV}^* \rangle}{\sqrt{\langle S_{HH} S_{HH}^* \rangle \langle S_{VV} S_{VV}^* \rangle}} \right|. \tag{7}$$

Co-polarization correlation angle:

$$\angle\rho = \angle(\langle S_{HH} S_{VV}^* \rangle). \tag{8}$$

The relative kurtosis is a measure of non-Gaussianity. Distributions with high kurtosis tend to have a sharp peak close to the mean, drop quickly and have heavy tails. The relative kurtosis equals one for Gaussian data. The brightness feature represents the total intensity of the multivariate backscatter. Here we have use the geometric mean brightness rather than the span. Both represent the multivariate total intensity. The co-polarization ratio has been shown to be good at separating open water from thin-ice types. Its value is determined by the ice dielectric constant. The largest ratio is observed for open water and new ice, while first-year and multi-year ice have values

of ~ 1 [5], [6].
In [6] the HV channel was found to perform very well in discriminating open water and ice. We have defined the cross-polarization ratio as the ratio of cross-pol intensity to geometric brightness. This ratio gives an estimate of the amount of depolarization, and is useful for discriminating ice type and determining ice age. The interpretation of the co-polarization correlation magnitude in sea ice research is yet to be determined [5], but [7] does indicate that it relates to both salinity and incidence angle. The co-polarization correlation angle has been shown to be useful for the classification and (proxy) thickness estimation of thin ice types (i.e., $<\sim 0.3$m) [8], [9]. Its value is determined by the water and ice dielectric constants.

The basic idea is to transform these six features, such that they have symmetric and Gaussian-like marginal probability density functions, and to use a multivariate Gaussian mixture model to segment the image into a given number of unlabeled segments [4]. The features were transformed as follows; we use the reciprocal of the relative kurtosis; the next three were logaritmically transformed, the last two were not transformed at all. The number of classes input to the algorithm was manually estimated based on optical images, the Pauli image, the sea ice observation log, and the segmentation results obtained with different number of classes.

Before comparing to the manually classified images consisting of hand-drawn polygons, the segmented image was postprocessed using a majority voting filter with window size 3 by 3 pixels, applied twice, to smooth/clean the segments. Since the manually classified images were in a geocoded format, we also geocoded the automatically segmented image to enable a pixel-to-pixel comparison. The smoothed, geocoded segmentation result is shown in Fig. 2.

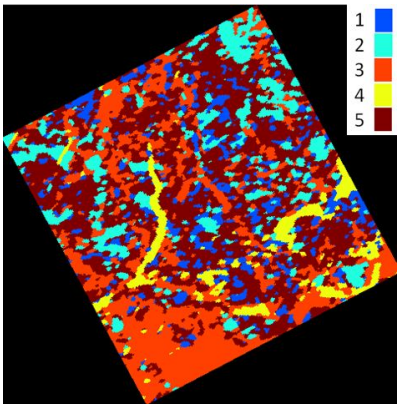

Figure 2. Image segmented by the automated segmentation algorithm, with the number of classes equal to five.

EM-Bird thickness measurements and optical photos were used to interpret the segments. There is a time span of 1 h 46 min between the satellite image aquisition and the last EM-bird measurement. The ice drift during this period is signficant. Drift measurements from the GPS trackers and the buoy were utilized for ice drift correction. Fig.3 shows a Pauli image annotated with the original (red) and corrected (white) helicopter track. Sea Ice Experts interpreted the segmentation result aided by thickness measurements, optical photos and the Pauli image.

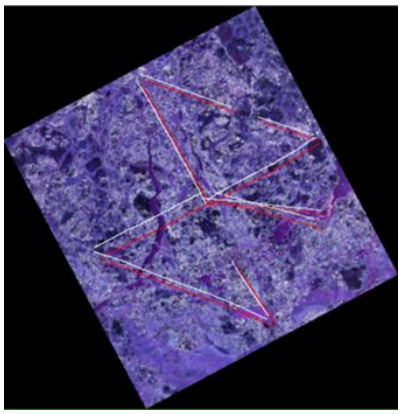

Figure 3. Polarimetriy image shown as Pauli colours. The original helicopter track is shown in red and the ice drift corrected track in white.

2.3. Manual segmentation and classification

The quad-polarisation Radarsat-2 image from 12 April was analysed manually by ice analysts at the Norwegian Ice Service. As part of an exercise to evaluate the differences in interpretation between the analysts, the image was assessed independently by 2 analysts. Since ice concentrations in the area were near 100%, the analysts were told to concentrate on determining the stage of ice development, and the ice type. The image was presented as both radar backscatter coefficient σ_0 in a colour composite (RGB) constructed from the VV, HV and HH channels, and as a Pauli decomposition. To aid the interpretation the analysts were able to refer to the shipboard ice log and photographs from the Norwegian Coastguard Vessel (NoCGV) Svalbard concurrently with the satellite images. Areas with similar visual appearance in the backscatter and Pauli images were distinguished by eye, and a polygon drawn manually with the geographic information system (GIS) software.
Use of the GIS allows an ice type attribute to be applied to the polygon and this is used to determine the colouring of the final ice chart. Since the interest was in ice type, the colours used in presentation are those defined by for standard World Meteorological Organization (WMO) stage of development ice charts. The manually classified images composed by analyst 1 and 2 are shown in Figs. 5 and 6, respectively, and the legend in Fig. 4. Because interpretation of the images is subjective and depends on the analyst's experience, there was some variation in the classifications, particularly for new and young ice types.

Figure 4. Legend to the manual classifications

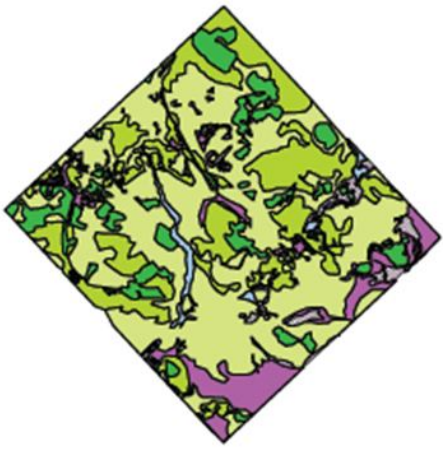

Figure 5. Manual classification performed by analyst 1

2.4. Intercomparison of hand drawn ice charts and automated segmentation

A pixel-to-pixel comparison between firstly the two manual classifications, and then each of the manual classifications and the automatic segmentation, was done by making confusion matrices. In our case, each column of the confusion matrix represents one class in one image, and each row represents one class in the other image to be compared. By inspecting the confusion matrix we can tell how labels in one image relate to the labels in the other image, and measure various types of accuracy and error rates between the two. All the numbers in the confusion matrices are percentages of the total number of pixels.

3. RESULTS

3.1. Intercomparisons of manually classified images and the automatic segmentation

Comparison of the two hand-drawn ice charts
A visual inspection of the two manually classified ice-charts gives the impression that they do not agree very well. Both the labeling and the segments differ. A more detailed exploration reveal some similar segments (i.e., the purple segment at the bottom corner and the lead in the middle of the image). If we take the labels into consideration we see that all the green labels and the yellow one are first-year ice. From a SAR imaging point-

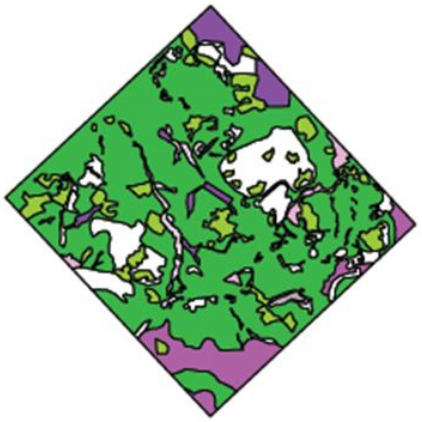

Figure 6. Manual classification performed by analyst 2

of-view, it is not possible to disinguish these classes by only looking at the Pauli image. Merging these first-year ice classes would make the ice charts even more similar. All pixels in the "Ice of undefined stage of development" ice chart of analyst 2 -ice chart were discarded before the pixel-to-pixel comparison. From the confusion matrix in Fig. 7 we are able to see a one-to-one correspondance between the classes. The analysts respectively label 9.3% and 7.7% ofthe pixels as class 6, and this labeling is consistent for 6.1 % of the pixels. It is also worth noticing that the biggest classes (class 9, First stage First Year, in analyst 1's chart and class 11, Medium First Year, in analyst 2's chart) correspond very well, which makes sense considering that both labels represent first year ice.

		Analyst 1						
		1	6	9	10	11	17	
Analyst 2	2	1.1%	0.1 %	0.3 %	0.2 %	0.1 %	0.0 %	1.8 %
	3	0.8 %	0.0 %	0.1 %	0.2 %	0.0 %	0.5 %	1.6 %
	4	0.0 %	0.5 %	0.5 %	3.2 %	0.6 %	0.1 %	4.9 %
	6	0.0 %	**6.1 %**	0.7 %	0.8 %	0.1 %	0.1 %	7.7 %
	8	0.1 %	0.4 %	1.0 %	2.2 %	7.4 %	0.2 %	11.2 %
	11	0.4 %	2.3 %	**53.2 %**	12.5 %	2.2 %	1.8 %	72.5 %
	17	0.0 %	0.0 %	0.0 %	0.0 %	0.0 %	0.3 %	0.3 %
		2.5 %	9.3 %	55.7 %	19.0 %	10.4 %	3.1 %	100 %

Figure 7. Confusion matrix for hand-drawn ice charts.

Comparison of Analyst 1's ice chart and the automatic segmentation
The confusion matrix in Fig. 8 reveals that the majority of the pixels in class 1, 4 and 5 of the automatic segmentation are mapped into the dominant class 9 of the hand-drawn ice chart. This shows that the manual clasifcation and the automated sementation are inconsistent. The reason for this many-to-one mapping could be that the hand-drawn polygons have rough class boundaries and poor detail. More importantly, we are convinced that the automated algorithm interprets the image information more rigorously, thus distinguishing more classes.

Comparison of Analyst 2's ice chart and the automatic

		Automated segmentation					
		1	2	3	4	5	
Analyst 1	1	0.1 %	0.0 %	2.0 %	0.1 %	0.1%	2.3 %
	6	0.4 %	0.4 %	0.6 %	6.8 %	0.7 %	8.9 %
	9	**6.4 %**	1.4 %	1.3 %	**14.5 %**	**27.3 %**	51.0 %
	10	2.9 %	3.9 %	0.4 %	4.3 %	12.1 %	23.4 %
	11	0.5 %	7.2 %	0.1 %	0.8 %	2.3 %	10.8 %
	17	0.4 %	0.3 %	1.8 %	0.7 %	0.4 %	3.6 %
		10.6 %	13.2 %	6.3 %	27.1 %	42.8 %	100 %

Figure 8. Confusion matrix for automated segmentation and analyst 1's ice chart.

segmentation
The last comparison was between the ice chart by analyst 2 and our automatically segmented image. The corresponding confusion matrix is shown in Fig. 9. We clearly see the same tendency as we in the previous comparison. Now the classes 1, 4 and 5 in the automatic segmentation are mapped into the dominanting class 11, known to correspong with class 9 of analyst 1. Again we conclude that the manual classification and the automatic segmentation are inconsistent.

		Automated segmentation					
		1	2	3	4	5	
Analyst 2	2	0.2 %	0.1 %	1.3 %	0.1 %	0.2 %	1.8 %
	3	0.1 %	0.2 %	1.3 %	0.0 %	0.0 %	1.6 %
	4	0.3 %	1.5 %	0.0 %	1.8 %	1.3 %	4.9 %
	6	0.1 %	0.1 %	0.3 %	7.0 %	0.3 %	7.7 %
	8	0.7 %	7.7 %	0.3 %	0.5 %	2.0 %	11.1 %
	11	**9.5 %**	2.4 %	2.6 %	**18.8 %**	**39.2 %**	72.5 %
	17	0.0 %	0.0 %	0.3 %	0.0 %	0.0 %	0.3 %
		10.8 %	12.0 %	6.1 %	28.2 %	42.9%	100 %

Figure 9. Confusion matrix for automated segmentation and analyst 2's ice chart.

3.2. Validation and interpretation of automated segmentation

After establishing that the manual classificationas are inconsistent with the automatic segmentation, the question is which one is closest to the true physical ice types. The manually classified ice charts are very reliant on the analyst and the available amount of ground truth. On the other hand the segments of the automatic algorithm need to be labeled. In order to do the latter, we presented sea ice experts from the Norwegian Polar Institute with the available ground truth data and the automated segmentation. The segment descriptions they produced are presented in Table 1. The sea ice experts were not able to distinguish the brown, blue and light blue segments by just inspecting the optical photos. By also including the Pauli image, they agreed that the light blue segments also were separable from the other classes.

Blue/Brown/Light Blue	first year ice, different stages of development
Red	Young ice, thin first year ice (sometimes deformed and with snow cover)
Yellow	Thin ice, open water, new ice, nilas, grey ice

Table 1. Class labels produced by sea ice experts

A further investigation of the class-discriminating issue was carried out by utilizing the physical information in the polarimetric features used in the segmentation algorithm. Our main focus was to investigate whether the features were able to separate the three classes: brown, blue and light blue, that were not separable according to the sea ice experts. We calculated two robust statistics, the median and the median absolute deviation (MAD), for each class and for each of the six features. The result is shown in Fig. 10. All of the features, especially the copol ratio did separate the yellow class (open water/thin ice) very well, see Fig. 10 d) . The brightness feature clearly separates the light blue class from the blue and the brown. The light blue is the darkest class, which is also apparent in the Pauli image, just as the sea ice experts pointed out. A dark area in the Pauli image is interpreted as a smooth surface, and the darker the smoother.
The cross-pol ratio value is higher the more deformed the ice is. Fig. 10 c) indicates that the dark blue is the most deformed ice, and it is well separated from the light blue and the brown. The light blue class has the lowest value of the three we consider, which means that it is less deformed than the blue and brown, which again is consistent with what we found by inspecting the brightness feature.
Fig. 10 a) displays the inverse non-Gaussianity feature, the segments to the right are more Gaussian than those to the left. The yellow class, open water/thin ice, is more Gaussian than the blue, deformed ice class. The inverse non-Gaussianity feature separates the blue, light blue and brown classes. The separation is also very clear in the copol correlation phase and - magnitude plots, see Figures 10 e) and 10 f). The physical interpretation for thick and deformed ice classes is still to be investigated.
The probability density functions (pdf) for all the features are shown in Figure 11. These plots shows basically the same as the scatterplots in Figure 10, except that the brightness and the copol-ratio, Figures 11 b) and 11 d), showed that the yellow class (open water and thin ice) was bimodal.

4. SUMMARY AND CONCLUSIONS

Our comparison between manually segmented ice charts has revealed the existence of analyst and ground-truth

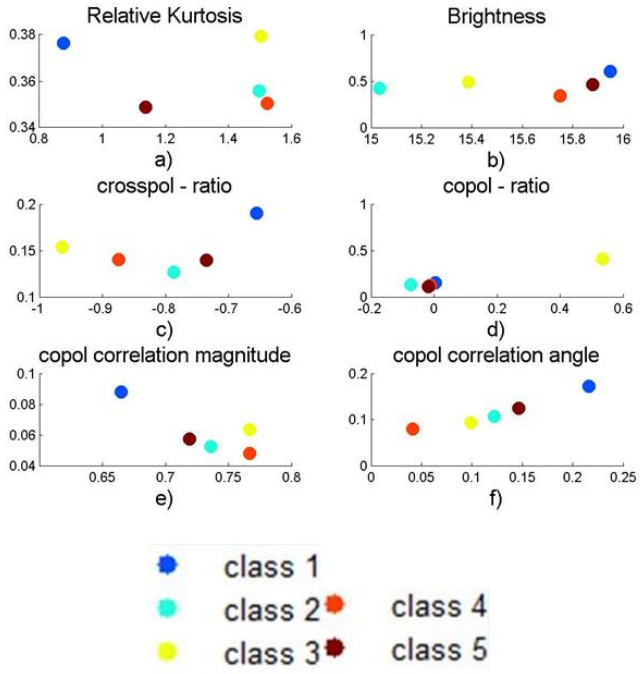

Figure 10. Scatter plots that shows the median values along the x-axis and MAD-values along the y-axis for each class and each feature.

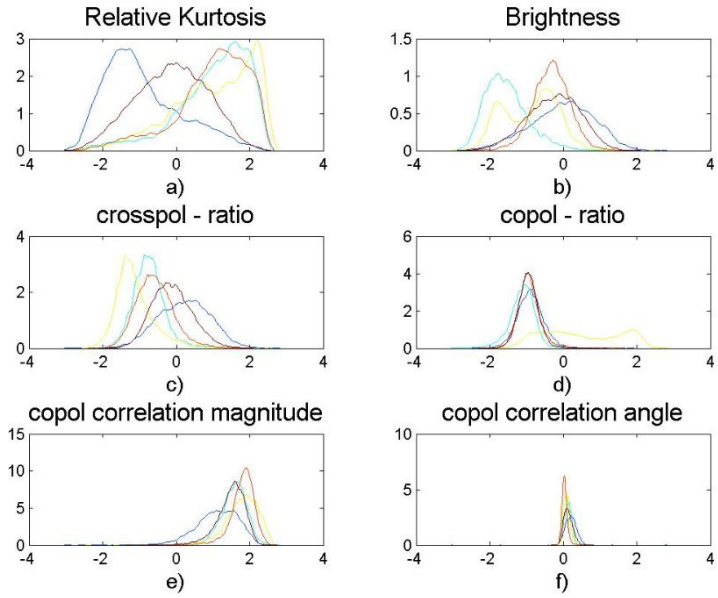

Figure 11. Probability density functions for each class and each feature. Colors corresponds to colors in legend in Fig. 10

dendency of the resulting ice charts. Automating this process will make the ice charts more objective. We have characterized the segments found by the segmentation algorithm in terms of ice thickness and type, the sea ice experts recognized three classes looking at optical images and four classes by also including the pauli image. Our segmenatation algorithm distinguishes five classes, and an investigation of polarimetric features support this. We believe that our segmentation algorithm sees more details and detects more classes, that in turn seem to reflect real ice types. The bimodality shown for class 3 (yellow), we believe, stem from a mixture of true classes, this can be further explored by expanding the number of classes in the segmentation algorithm.

ACKNOWLEDGMENTS

The authors acknowledge Thomas Kræmer at the University of Tromsø for advice in the geocoding process, the crew onboard the NoCG Svalbard and the pilots onboard the Governor of Svalbard's OCO Dauphin for their assistance during the research cruise. We also thank the Fram Centre, Tromsø, Norway and RDA Troms for funding.

REFERENCES

[1] J-S Lee and E. Pottier. *Polarimetric Radar Imaging, from basics to applications*. Taylor & Francis Group, 2009.

[2] J.P.S.Gill and J.J. Yackel. Evaluation of C-band SAR polarimetric parameters for discriminating of first-year sea ice types. *Can. J. Remote Sens.*, 38(3), pp. 306–323, 2012 and references therein.

[3] C. Haas, J. Lobach, S. Hendricks, L. Rabenstein, and A. Pfaffling. Helicopterborne measurements of sea ice thickness, using a small and lightweight, digital em system. *J. Appl. Geophys.*, 67(3), pp. 234–241, 2009.

[4] A.P. Doulgeris and T. Eltoft. Scale mixture of gaussian modelling of polarimetric SAR data. *EURASIP J. Adv. Signal Processing*, pp. 1–12, 2010.

[5] R. G. Onsott and R. A. Shuchman. Synthetic aperture radar marine user's manual. In C.R. Jackson and J. R. Apel, eds., *SAR measurements of sea ice*, pp. 81–115. NOAA, 2004.

[6] B. Scheuchl, R. Caves, I. Cumming, and G. Staples. Automated sea ice classification using spaceborne polarimetric SAR data. In *Proc. IGARSS 2001*, pp. 3117–3119, 2001.

[7] M. R. Drinkwater, R. Kwok, E. Rignot, H. Israelsson, R. G. Onstott, and D. P Winebrenner. Potential applications of polarimetry to the classification of sea ice. In F. D. Carsey, editor, *Microwave remote sensing of sea ice*, pp. 419–430. AGU, 1992.

[8] B.B. Thomsen, S.V. Ngheim, and R. Kwok. Polarimetric C-band SAR observations of sea ice in the Greenland Sea. In *Proc. IGARSS 1998*, pp. 2502–2504, 1998.

[9] B.B. Thomsen, L.T. Pedersen, H. Skriver, and W. Dierking. Polarimetric EMISAR observations of sea ice in the Greenland Sea. In P. Gudmandsen, editor, *Future Trends in Remote Sensing*, pp. 345–351. Taylor & Francis, 1998.